Lattice QCD study of the Boer-Mulders effect in a pion

M. Engelhardt, P. Hägler, B. Musch, J. Negele, and A. Schäfer

Phys. Rev. D **93**, 054501 — Published 1 March 2016

DOI: 10.1103/PhysRevD.93.054501

Lattice QCD study of the Boer-Mulders effect in a pion

M. Engelhardt,[1] P. Hägler,[2] B. Musch,[2] J. Negele,[3] and A. Schäfer[2]

[1]*Department of Physics, New Mexico State University, Las Cruces, NM 88003, USA*
[2]*Institut für Theoretische Physik, Universität Regensburg, Regensburg, Germany*
[3]*Center for Theoretical Physics, Massachusetts Institute of Technology, Cambridge, MA 02139, USA*

The three-dimensional momenta of quarks inside a hadron are encoded in transverse momentum-dependent parton distribution functions (TMDs). This work presents an exploratory lattice QCD study of a TMD observable in the pion describing the Boer-Mulders effect, which is related to polarized quark transverse momentum in an unpolarized hadron. The primary goal is to gain insight into the behavior of TMDs as a function of a Collins-Soper evolution parameter, $\hat{\zeta}$, which quantifies the rapidity difference between the hadron momentum and a vector describing the trajectory of the struck quark, e.g., in a semi-inclusive deep inelastic scattering (SIDIS) process. The lattice calculation, performed at the pion mass $m_\pi = 518\,\mathrm{MeV}$, utilizes a definition of TMDs via hadronic matrix elements of a quark bilocal operator with a staple-shaped gauge connection; in this context, the evolution parameter is related to the staple direction. By parametrizing the aforementioned matrix elements in terms of invariant amplitudes, the problem can be cast in a Lorentz frame suited for the lattice calculation. Aided by the lower mass of the pion, compared to the nucleon studied previously, the present investigation of pion TMD observables constitutes an important step towards the quantitative study of the physically important regime of large relative rapidity where the dependence on $\hat{\zeta}$ appears to approach a limit. Although matching to perturbative evolution equations in $\hat{\zeta}$ is not yet available, extrapolations based on ansätze containing inverse powers of $\hat{\zeta}$ yield stable results with an uncertainty as low as 20%, and both upper and lower bounds for the asymptotics are obtained. In passing, the similarity between the Boer-Mulders effects extracted in the pion and the nucleon is noted.

I. INTRODUCTION

Transverse momentum-dependent parton distributions (TMDs) [1] constitute one of the pillars on which the three-dimensional tomography of hadrons rests. Together with the three-dimensional spatial information derived from generalized parton distributions (GPDs), they permit a comprehensive reconstruction of hadron substructure and thus have a bearing on seminal topics in hadron physics, such as orbital angular momentum contributions to nucleon spin, or spin-orbit correlations in hadrons. Through the selection of particular parton spin and transverse momentum components, a variety of effects can be probed, including naively time-reversal odd (T-odd) quantities such as the Sivers and Boer-Mulders functions; these only exist by virtue of initial or final state interactions in corresponding physical processes, introducing a preferred chronology in the description of the process. For example, in semi-inclusive deep inelastic scattering (SIDIS), the operative element is final-state interactions between the struck quark and the hadron remnant; on the other hand, in the Drell-Yan (DY) process, initial state interactions before the lepton pair production enable T-odd effects. TMDs thus in general have to be considered in the context of specific physical processes, within a factorization framework appropriate for the process in question, separating the hard reaction from the TMD and other elements such as fragmentation functions. In the case of T-odd effects, the process-dependence manifests itself in the prediction of a sign change of the Sivers and Boer-Mulders functions between the SIDIS and DY processes [2].

In view of the fundamental importance of TMDs and the rich spectrum of effects that can be probed, TMDs have been, and continue to be the target of a variety of experimental efforts. Deep-inelastic scattering experiments performed by COMPASS [3], HERMES [4] and Jefferson Lab [5] have yielded TMD data including evidence for the T-odd Sivers effect. Complementary Drell-Yan experiments at COMPASS [6] and Fermilab [7] are envisaged, which could, in particular, test the aforementioned sign change between the SIDIS and DY processes. Related transverse single-spin asymmetries have been measured at RHIC in polarized proton-proton collisions [9]. Further experimental efforts at RHIC are projected to provide insight into strong QCD evolution effects expected for the Sivers TMD [8]. TMDs furthermore constitute a central focus of the proposed Electron-Ion Collider facility [10].

To complement these efforts, providing nonperturbative QCD input from first principles to the analysis of TMD effects, a project to calculate TMD observables within lattice QCD was initiated and developed in [11–13]. The present work constitutes a continuation of this project. As described in detail below, the formal definition of TMDs is based on nonlocal operators, specifically quark bilocal operators with a gauge connection that takes the shape of a staple. The path followed by the gauge connection is in principle infinite in length, and thus it cannot be straightforwardly treated in terms of an operator product expansion, as is commonly done, e.g., for ordinary parton distributions or generalized parton distributions. In view of this genuinely nonlocal character of the operators, lattice

QCD explorations of corresponding hadronic matrix elements directly at the nonlocal operator level were undertaken in [11, 12], concentrating initially on the simpler case of straight gauge links connecting the quark operators. The nonlocal nature of the operators in particular raises novel questions regarding regularization and renormalization, which were addressed in considerable detail in [12]. Whereas these questions deserve further study, the aforementioned explorations suggest that it is a viable working assumption to treat nonlocal lattice operators in analogy to the fashion in which they are treated in continuum QCD [14], namely, by absorbing divergences into multiplicative soft factors. These soft factors can then be canceled in appropriate ratios; this scheme was used to construct TMD observables in the subsequent investigation [13], and will be used in the present work. Formally related studies of nonlocal lattice operators, in which a gauge link in the (Euclidean) time direction originates from the propagation of a heavy auxiliary quark, have been carried out in [15]; also, a direct approach to light-cone distribution amplitudes based on nonlocal lattice operators was laid out in [16]. Moreover, the comprehensive framework for investigating parton physics within lattice QCD put forward in [17] and developed and explored in [18–20] relies on a direct treatment of such nonlocal lattice operators.

The present work focuses on a TMD observable related to the Boer-Mulders effect in a pion. Lattice QCD studies of pion structure, predominantly focusing on form factors, have been previously reported in [21–29]. Choosing the pion as the hadron state is motivated by the principal goal of the investigation presented here, namely, understanding the behavior of TMDs as a function of an evolution parameter quantifying the rapidity difference between the hadron momentum and a vector describing the trajectory of the struck quark. Details are furnished further below. In the previous nucleon study [13], no definite conclusions regarding the limit of large rapidity difference proved possible. By virtue of its lower mass, the pion provides a larger rapidity difference at given momentum, and this choice of hadron state thus aids in approaching the limit of physical interest. In addition, the spinless nature of the pion permits additional spatial averaging to suppress statistical uncertainties. Indeed, the chief advance of the present work lies in providing quantitative numerical insight into the limit of large evolution parameter, despite the present lack of analytical perturbative matching equations which would permit a more in-depth understanding of that limit. Preliminary accounts of this work were given in [30–32].

II. DEFINITION OF TMD OBSERVABLES

A. Correlation functions

Quark transverse momentum-dependent parton distributions (TMDs) can be defined in terms of the fundamental correlator

$$\widetilde{\Phi}^{[\Gamma]}_{\text{unsubtr.}}(b,P,\ldots) \equiv \frac{1}{2}\langle P|\ \bar{q}(0)\ \Gamma\ \mathcal{U}[0,\eta v,\eta v+b,b]\ q(b)\ |P\rangle \quad , \tag{1}$$

where P denotes the momentum of the hadron state; the present work focuses on pions, and thus no spin is attached to the state. Γ represents an arbitrary Dirac γ matrix structure. The quark operators at positions 0 and b are connected by the gauge link $\mathcal{U}[0,\eta v,\eta v+b,b]$, which connects the points listed in its argument by straight-line segments; thus, the gauge link has the shape of a staple, cf. Fig. 1, with the unit vector v specifying the staple direction and η its length. One is ultimately interested in the limit $\eta\to\infty$, which in a concrete lattice calculation is of course reached by extrapolation. This gauge link form incorporates final state interactions between the struck quark and the hadron remnant in semi-inclusive deep inelastic scattering (SIDIS) [33], and analogously initial state interactions in the Drell-Yan process (DY). The ellipsis in the argument of $\widetilde{\Phi}^{[\Gamma]}_{\text{unsubtr.}}$ indicates that the correlator will depend on various further parameters, related, e.g., to regularization, specified below as needed.

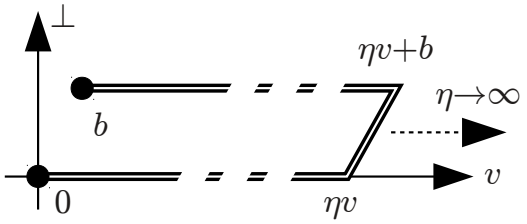

FIG. 1: Gauge link structure $\mathcal{U}[0,\eta v,\eta v+b,b]$ in the correlator (1). In a concrete lattice calculation, the limit $\eta\to\infty$ has to be taken numerically.

Fourier transformation of (1),

$$\Phi^{[\Gamma]}(x,k_T,P,\ldots) \;=\; \int \frac{d^2b_T}{(2\pi)^2}\int\frac{d(b\cdot P)}{(2\pi)P^+}\exp\left(ix(b\cdot P)-ib_T\cdot k_T\right)\,\frac{\widetilde{\Phi}^{[\Gamma]}_{\text{unsubtr.}}(b,P,\ldots)}{\widetilde{\mathcal{S}}(b_T^2,\ldots)}\,\Bigg|_{b^+=0} \tag{2}$$

leads to the momentum space correlator $\Phi^{[\Gamma]}$, which ultimately will be parametrized in terms of TMDs, cf. below. The position space correlator (1), as written, requires regularization not only of the quark operator self-energies, but also of the self-energy of the Wilson line (this is indicated by the subscript "unsubtr."). The regularization of the latter is effected by dividing by the soft factor $\widetilde{\mathcal{S}}$. The detailed structure of the soft factor depends on the concrete factorization approach employed. For example, in the scheme developed in [14, 34], which, for reasons discussed further below, provides the phenomenological framework for the present study, the soft factor takes the form

$$\widetilde{\mathcal{S}}(b_T^2,\ldots)=\sqrt{\frac{\tilde{S}_{(0)}(b_T,+\infty,-\infty)\tilde{S}_{(0)}(b_T,y_s,-\infty)}{\tilde{S}_{(0)}(b_T,+\infty,y_s)}} \tag{3}$$

where $\tilde{S}_{(0)}(b_T,\ldots)$ is a vacuum expectation value of Wilson line structures extending, initially, into space-like directions; some of them remain at finite rapidity y_s, whereas others are taken to the light-cone limit, i.e., infinite rapidity. This particular form of the soft factor, containing more than one rapidity, cannot be cast in a Lorentz frame in which it exists at a single time, and for this reason, it is not suited for evaluation within lattice QCD. However, the observables that will be defined further below are ratios in which the soft factors cancel [13]. There is, therefore, no obstacle to evaluating those observables within lattice QCD, and the detailed form of the soft factor is immaterial. An alternative construction of TMD soft factors which, in principle, is amenable to lattice QCD evaluation has been put forward in [19] within the framework laid out in [17].

As written in (2), the transverse components b_T of the quark separation b are Fourier conjugate to the quark transverse momentum k_T, while the longitudinal component $b\cdot P$ is Fourier conjugate to the longitudinal momentum fraction x. The present work will be confined to the case $b\cdot P=0$, corresponding to evaluating the integral with respect to x over the correlator $\Phi^{[\Gamma]}$ and TMDs derived from it. It should be stressed, however, that there is no obstacle to extending calculations of the type presented here to a scan of the $b\cdot P$-dependence[1], yielding upon Fourier transformation the x-dependence of $\Phi^{[\Gamma]}$ and the TMDs under consideration. Studies of the $b\cdot P$-dependence in the straight gauge link ($\eta v=0$) case have already been carried out in [12], and further investigations in this direction are planned for future work. A related proposal to obtain the x-dependence of parton distributions has been put forward and explored in [17–20].

Finally, (2) is evaluated at $b^+=0$, in accordance with the standard phenomenological framework, which employs a Lorentz frame in which the hadron of mass m_h propagates with a large momentum in 3-direction, $P^+\equiv(P^0+P^3)/\sqrt{2}\gg m_h$; then, the quark momentum components scale such that the correlator (2) and TMDs derived from it are principally functions of the quark longitudinal momentum fraction $x=k^+/P^+$ and the quark transverse momentum vector k_T, whereas the dependence on the component $k^-\equiv(k^0-k^3)/\sqrt{2}\ll m_h$ becomes irrelevant in this limit. Correspondingly, (2) is regarded as having been integrated over k^-, implying that the conjugate variable b^+ is to be set to zero, as written.

Before continuing with the parametrization of $\Phi^{[\Gamma]}$ in terms of TMDs, it is important to note a further specification with respect to the staple direction v. The Wilson lines along the legs of the staple represent an effective, resummed description of gluon exchanges between, in the case of SIDIS, the struck quark and the hadron remnant [33]. Accordingly, their direction v should be taken to follow the path of the ejected quark, close to the light cone from the point of view of the hadron. Whereas, at tree level, there is no obstacle to the most straightforward choice, namely, a light-like v, beyond tree level, this choice is associated with rapidity divergences [35]. Various schemes have been advanced to treat these divergences [14, 34, 36, 37], and the equivalence between some of them discussed in [38]. In particular, the scheme advanced in [14, 34] effects regularization by tilting the staple direction v slightly off the light cone into the spacelike region. This feature is crucial for a concrete implementation of a lattice QCD evaluation of matrix elements of the type (1), as will be detailed further below. Thus, the phenomenological framework providing the backdrop for the present treatment is, specifically, the one advanced in [14, 34]. Choosing v to be spacelike for the purposes of regularization implies a dependence of the calculation on an additional parameter, characterizing proximity of the

[1] In a practical calculation, the range of accessible $b\cdot P$ is limited by the available b and P, $|b\cdot P|\leq|\mathbf{P}|\sqrt{-b^2}$ (where $\mathbf{P}$ denotes the spatial momentum), leading to an increasing systematic uncertainty at small x.

staple to the light cone. Here, this parameter will be chosen as

$$\hat{\zeta} = \frac{v \cdot P}{|v||P|} \ , \tag{4}$$

where the absolute length of a four-vector w is denoted by $|w| = \sqrt{|w^2|}$. In terms of $\hat{\zeta}$, the light-cone limit corresponds to $\hat{\zeta} \to \infty$. The generated lattice data thus have to be extrapolated to the double limit $\eta \to \infty$, $\hat{\zeta} \to \infty$, i.e., the limit of infinite staple length, and staple direction converging toward the light cone.

Alternative to this purely kinematic characterization, also the parameter $\zeta = 2m_h\hat{\zeta}$ is frequently employed [39], and viewed as a dynamical scale, to be compared to Λ_{QCD}; perturbative evolution equations in ζ can then be derived at sufficiently large ζ, cf., e.g., [40]. The question whether one has reached the asymptotic regime appropriate for the definition of TMDs presumably has both kinematic and dynamical aspects. The applicability of perturbation theory, e.g., for determining evolution equations is a dynamical issue most adequately characterized by considering the dimensionful parameter ζ in relation to the characteristic QCD scale, i.e., requiring $\zeta \gg \Lambda_{QCD}$. On the other hand, this by itself does not necessarily guarantee kinematics close to the light cone, $\hat{\zeta} \gg 1$. Presumably, both conditions need to be taken into account in general. In the present work, no quantitative connection to perturbative evolution is attempted; the numerical data do not reach values of ζ which lie clearly within the perturbative regime. The maximum spatial momentum employed is 1.17 GeV, and the maximum value of ζ is $\zeta = 2.1$ GeV, corresponding to $\hat{\zeta} = 2.03$. Instead, the dependence of the lattice data on the kinematical variable $\hat{\zeta}$ will be studied empirically, including exploration of ad hoc ansätze for the large-$\hat{\zeta}$ behavior, allowing for corresponding extrapolations. Characterizing the large-$\hat{\zeta}$ limit is in fact the primary goal of the present investigation. This limit was seen to present a considerable challenge in the previous study [13], which considered nucleon TMDs; no definite statements concerning the large-$\hat{\zeta}$ behavior proved possible. The present work, focusing on pions, permits accessing higher $\hat{\zeta}$ both by virtue of the lighter hadron mass (note that the hadron mass enters the denominator of (4)), and by employing additional spatial averaging facilitated by the spinless nature of the pion, enhancing statistics. As will be seen further below, the data extracted in the present investigation are of sufficient quality to yield a signal for the $\hat{\zeta} \to \infty$ limit of the generalized Boer-Mulders shift defined in eq. (23) below. This constitutes the main advance of this work.

B. Parametrizations

Returning to the momentum space correlator $\Phi^{[\Gamma]}$, its parametrization in terms of the relevant Lorentz structures yields, at leading twist,

$$\Phi^{[\gamma^+]}(x, k_T, P, \ldots) \ = \ f_1(x, k_T, P, \ldots) \tag{5}$$

$$\Phi^{[i\sigma^{i+}\gamma^5]}(x, k_T, P, \ldots) \ = \ -\frac{\epsilon^{-+ij}k_j}{m_\pi} h_1^\perp(x, k_T, P, \ldots) \ . \tag{6}$$

For spinless particles such as the pion, there are only two leading twist TMDs, in contrast to the eight which arise for spin-$\frac{1}{2}$ particles [41–43]. The TMD f_1 is simply the unpolarized quark distribution, whereas the Boer-Mulders function [44] $h_1^\perp$ encodes the distribution of transversely polarized quarks in the pion. The Boer-Mulders function is odd under time reversal (T-odd). Physically, it only exists by virtue of the final and initial state interactions, in the SIDIS and DY processes, respectively, which break the symmetry of the processes under time reversal. Formally, it is the introduction of the additional vector v describing the staple direction in the staple-shaped gauge link which breaks the symmetry; the Boer-Mulders function vanishes for a straight gauge link, $\eta v = 0$. Correspondingly, the generalized Boer-Mulders shift defined in eq. (23) below will be an odd function of v.

On the other hand, one can also decompose the position space correlator $\widetilde{\Phi}^{[\Gamma]}_{\text{unsubtr.}}$ into invariant amplitudes [13]. The general decomposition is (the combinations corresponding specifically to the leading twist TMDs (5) and (6) will be considered further below):

$$\frac{1}{2}\widetilde{\Phi}^{[\mathbb{1}]}_{\text{unsubtr.}} \ = \ m_\pi \widetilde{A}_1 \tag{7}$$

$$\frac{1}{2}\widetilde{\Phi}^{[\gamma^\mu]}_{\text{unsubtr.}} \ = \ P^\mu \widetilde{A}_2 - im_\pi^2 b^\mu \widetilde{A}_3 + \frac{m_\pi^2}{v \cdot P} v^\mu \widetilde{B}_1 \tag{8}$$

$$\frac{1}{2}\widetilde{\Phi}^{[\gamma^\mu\gamma^5]}_{\text{unsubtr.}} \ = \ \frac{im_\pi^2}{v \cdot P}\epsilon^{\mu\nu\rho\sigma} P_\nu b_\rho v_\sigma \widetilde{B}_4 \tag{9}$$

$$\frac{1}{2}\widetilde{\Phi}^{[i\sigma^{\mu\nu}\gamma^5]}_{\text{unsubtr.}} \ = \ im_\pi \epsilon^{\mu\nu\rho\sigma} P_\rho b_\sigma \widetilde{A}_4 - \frac{m_\pi}{v \cdot P}\epsilon^{\mu\nu\rho\sigma} P_\rho v_\sigma \widetilde{B}_2 + \frac{im_\pi^3}{v \cdot P}\epsilon^{\mu\nu\rho\sigma} b_\rho v_\sigma \widetilde{B}_3 \tag{10}$$

The present treatment focuses on the special case $b \cdot P = 0$, which in the context of TMDs, defined in a frame in which $b^+ = 0$ and $v_T = P_T = 0$, also implies $b \cdot v = 0$ [13]. Under these constraints, the above relations are readily inverted. The amplitudes needed below are, explicitly,

$$\widetilde{A}_2 = \frac{1}{1+\hat{\zeta}^2}\frac{1}{2m_\pi^2}\left(P_\mu - \frac{v\cdot P}{v^2}v_\mu\right)\widetilde{\Phi}^{[\gamma^\mu]}_{\text{unsubtr.}} \tag{11}$$

$$\widetilde{B}_1 = \frac{\hat{\zeta}^2}{1+\hat{\zeta}^2}\frac{1}{2m_\pi^2}\left(P_\mu - \frac{m_\pi^2}{v\cdot P}v_\mu\right)\widetilde{\Phi}^{[\gamma^\mu]}_{\text{unsubtr.}} \tag{12}$$

$$\widetilde{A}_4 = i\frac{1}{1+\hat{\zeta}^2}\frac{1}{4b^2m_\pi^3}\left(P^\kappa - \frac{v\cdot P}{v^2}v^\kappa\right)b^\lambda\epsilon_{\kappa\lambda\mu\nu}\widetilde{\Phi}^{[i\sigma^{\mu\nu}\gamma^5]}_{\text{unsubtr.}} \tag{13}$$

$$\widetilde{B}_3 = -i\frac{\hat{\zeta}^2}{1+\hat{\zeta}^2}\frac{1}{4b^2m_\pi^3}\left(P^\kappa - \frac{m_\pi^2}{v\cdot P}v^\kappa\right)b^\lambda\epsilon_{\kappa\lambda\mu\nu}\widetilde{\Phi}^{[i\sigma^{\mu\nu}\gamma^5]}_{\text{unsubtr.}} \tag{14}$$

Note that $\widetilde{B}_1$ and $\widetilde{B}_3$ are regular for $v \cdot P \to 0$ owing to the $\hat{\zeta}^2$ prefactor. Of particular interest are the leading twist objects

$$\frac{1}{2P^+}\widetilde{\Phi}^{[\gamma^+]}_{\text{unsubtr.}} = \widetilde{A}_{2B} \tag{15}$$

$$\frac{1}{2P^+}\widetilde{\Phi}^{[i\sigma^{i+}\gamma^5]}_{\text{unsubtr.}} = -im_\pi\epsilon^{-+ij}b_j\widetilde{A}_{4B} \tag{16}$$

(where i, j denote transverse spatial indices), given in terms of the amplitude combinations

$$\widetilde{A}_{2B} = \widetilde{A}_2 + \left(1 - \sqrt{1+\hat{\zeta}^{-2}}\right)\widetilde{B}_1 \tag{17}$$

$$\widetilde{A}_{4B} = \widetilde{A}_4 - \left(1 - \sqrt{1+\hat{\zeta}^{-2}}\right)\widetilde{B}_3 \tag{18}$$

Also these combinations are regular for $\hat{\zeta} \to 0$ by virtue of the $\hat{\zeta}^2$ prefactors in (12),(14). Note that, in the case of vanishing spatial momentum, one cannot identify "forward" and "backward" directions for v; there is then only a single branch in $|\eta v|$, the sign of which is a matter of definition. Although only the combinations $\widetilde{A}_{2B}$ and $\widetilde{A}_{4B}$ appear in (15),(16), for the numerical analysis to follow, it will be valuable to be able to consider $\widetilde{A}_2$, $\widetilde{B}_1$, $\widetilde{A}_4$ and $\widetilde{B}_3$ individually, not just those combinations.

Given that $\widetilde{\Phi}^{[\Gamma]}_{\text{unsubtr.}}$ and $\Phi^{[\Gamma]}$ are related via a Fourier transformation, the quantities arising in the respective decompositions (5)-(6) and (15)-(16) must be similarly related, i.e., the amplitudes $\widetilde{A}_{iB}$ must be related to Fourier-transformed TMDs. Indeed, denoting x-moments of generic Fourier-transformed TMDs by

$$\tilde{f}^{[m](n)}(b_T^2,\ldots) = n!\left(-\frac{2}{m_h^2}\partial_{b_T^2}\right)^n\int_{-1}^1 dx\, x^{m-1}\int d^2k_T\, e^{ib_T\cdot k_T}\; f(x,k_T^2,\ldots) \tag{19}$$

$$= \frac{2\pi n!}{(m_h^2)^n}\int_{-1}^1 dx\, x^{m-1}\int d|k_T|\,|k_T|\left(\frac{|k_T|}{|b_T|}\right)^n J_n(|b_T||k_T|)f(x,k_T^2,\ldots) \tag{20}$$

where J_n denotes the Bessel functions of the first kind, one finds [13]

$$\tilde{f}_1^{[1](0)}(b_T^2,\hat{\zeta},\ldots,\eta v\cdot P) = 2\widetilde{A}_{2B}(-b_T^2, b\cdot P = 0, b\cdot v = 0, \hat{\zeta}, \eta v\cdot P)/\widetilde{\mathcal{S}}(b_T^2,\ldots) \tag{21}$$

$$\tilde{h}_1^{\perp[1](1)}(b_T^2,\hat{\zeta},\ldots,\eta v\cdot P) = 2\widetilde{A}_{4B}(-b_T^2, b\cdot P = 0, b\cdot v = 0, \hat{\zeta}, \eta v\cdot P)/\widetilde{\mathcal{S}}(b_T^2,\ldots) \tag{22}$$

Note the appearance of the soft factors on the right hand sides.

C. Boer-Mulders shift

As already indicated further above, one obtains an observable in which the soft factors cancel by forming a suitable ratio, namely, the "generalized Boer-Mulders shift"

$$\langle k_y\rangle_{UT}(b_T^2,\ldots) \equiv m_\pi\frac{\tilde{h}_1^{\perp[1](1)}(b_T^2,\ldots)}{\tilde{f}_1^{[1](0)}(b_T^2,\ldots)} = m_\pi\frac{\widetilde{A}_{4B}(-b_T^2,0,0,\hat{\zeta},\eta v\cdot P)}{\widetilde{A}_{2B}(-b_T^2,0,0,\hat{\zeta},\eta v\cdot P)} \tag{23}$$

Note that ratios of this type also cancel Γ-independent multiplicative field renormalization constants attached to the quark operators in (1) at finite physical separation b. It should be emphasized that the construction thus far is a continuum perturbative QCD construction. That this construction carries across into lattice QCD, i.e., that the lattice operators are similarly regularized and renormalized by multiplicative soft factors which cancel in ratios, is a working assumption which was already explored in considerable detail in [12], and which will be investigated further in future work. Physically, this assumption appears plausible at least at separations substantially larger than the lattice spacing, where the lattice operators are expected to approximate the corresponding continuum operators.

To interpret the generalized Boer-Mulders shift, note that the $b_T \to 0$ limit of the quantities defined in (20) formally corresponds to k_T^2-moments of TMDs,

$$\tilde{f}^{[m](n)}(0,\ldots) \;=\; \int_{-1}^{1} dx\, x^{m-1} \int d^2k_T \;\left(\frac{k_T^2}{2m_h^2}\right)^n \;f(x,k_T^2,\ldots) \tag{24}$$

Thus, in the formal $b_T \to 0$ limit, the generalized Boer-Mulders shift reduces to the "Boer-Mulders shift"

$$\langle k_y\rangle_{UT}(0,\ldots) = m_\pi \frac{\tilde{h}_1^{\perp[1](1)}(0,\ldots)}{\tilde{f}_1^{[1](0)}(0,\ldots)} = \left.\frac{\int dx \int d^2k_T\, k_y \Phi^{[\gamma^+ + s^j i\sigma^{j+}\gamma^5]}(x,k_T,P,\ldots)}{\int dx \int d^2k_T\, \Phi^{[\gamma^+ + s^j i\sigma^{j+}\gamma^5]}(x,k_T,P,\ldots)}\right|_{s_T=(1,0)} \tag{25}$$

which, in view of the structure of the right-hand side, formally takes the form of the average transverse momentum in y-direction of quarks polarized in the transverse ("T") x-direction, in an unpolarized ("U") pion, normalized to the corresponding number of valence quarks. This is in accord with the $(\mathbf{s}_T \times \mathbf{b}_T)\cdot\mathbf{P}$ structure of the correlator (16), where $\mathbf{s}_T$ represents the quark spin. The numerator in (25) sums over the contributions from quarks and antiquarks, whereas the denominator contains the difference between quark and antiquark contributions, thus giving the number of valence quarks [12, 45]. It should be noted, however, that the k_T^2-moments of TMDs (24) appearing in (25) are in general divergent [46] at large k_T and thus not well-defined absent further regularization. The generalized quantity (23) is a natural regularization, with finite b_T effectively acting as a regulator through the associated Bessel weighting, cf. (20). This Bessel weighting also is advantageous in the analysis of experimental asymmetries [47, 48]. In the present work, lattice QCD data for the generalized Boer-Mulders shift (23) will be obtained and presented at finite b_T. The path by which these data can be obtained proceeds via lattice QCD evaluation of the fundamental correlator (1) for a range of Dirac and staple link structures, extraction of the relevant invariant amplitudes (11)-(14), and construction of the ratio (23). As already mentioned further above, for this lattice QCD calculational scheme to be viable, it is necessary to employ a phenomenological framework such as the one advanced in [14, 34], in which all separations in the correlator (1) are spacelike, including the staple direction v. Such a scheme implies dependence on the Collins-Soper-type evolution parameter $\hat{\zeta}$, cf. (4), quantifying proximity of the staple to the light cone. The principal focus of the present investigation is, indeed, the dependence of the generalized Boer-Mulders shift on $\hat{\zeta}$, including its asymptotic $\hat{\zeta} \to \infty$ behavior.

III. LATTICE QCD CALCULATIONS

Lattice QCD employs a Euclidean time coordinate, serving to project out hadronic ground states via the associated exponentially decaying time evolution. As a consequence, when evaluating matrix elements of operators in hadronic states, no Minkowski time separations in those operators can be accomodated; one is restricted to operators which are defined at one single time. This is the reason why it is imperative to employ a framework in which all separations in the fundamental correlator (1) are spacelike. Only in this case is there no obstacle to boosting the problem to a Lorentz frame in which the operator in (1) exists at a single time, and performing the lattice calculation in that particular frame.

The decomposition of the resulting correlators into invariant amplitudes, cf. (11)-(14), is a further crucial element of the present treatment. Expressed in this fashion, the results of the lattice calculation are immediately applicable also in the original Lorentz frame in which (1) was initially defined. Finally, as already discussed above, the construction of ratios of amplitudes in which soft factors cancel serves to connect the results to phenomenological observables such as the generalized Boer-Mulders shift (23).

The lattice QCD data for the present exploration were obtained within a mixed action scheme employing domain wall valence quarks on an $N_f = 2+1$ dynamical asqtad quark gauge ensemble provided by the MILC collaboration [49]. Since the principal focus lies on understanding the systematics of the large $\hat{\zeta}$ limit, which proved inaccessible in previous investigations, a fairly high pion mass, $m_\pi = 518\,\mathrm{MeV}$, was chosen for this study to alleviate statistical fluctuations. Further details of the ensemble are given in Table I. This mixed action scheme, including the specific

$L^3 \times T$	a(fm)	$am_{u,d}$	am_s	$m_\pi^{\rm DWF}$ (MeV)	$m_N^{\rm DWF}$ (GeV)	#conf.	#meas.
$20^3 \times 64$	0.11849(14)(99)	0.02	0.05	518.4(07)(49)	1.348(09)(13)	486	3888

TABLE I: Parameters of the lattice ensemble. Note that the lattice spacing a was determined in a different scheme than in [50, 51], and consequently it, as well as the pion and nucleon masses quoted, differ slightly from the ones given in the aforementioned references [13]. The first error quoted for the pion and nucleon masses is statistical, the second stems from the conversion to physical units using a. The bare asqtad quark masses are denoted $m_{u,d,s}$. Eight measurements were made on each gauge configuration.

ensemble employed here, has been used extensively by the LHP Collaboration for studies of hadron structure, cf., e.g., [50, 51]. It also provided the basis for the previous nucleon TMD investigation reported in [13].

To extract the correlator (1), one evaluates both three-point functions $C_{\rm 3pt}$ and two-point functions $C_{\rm 2pt}$ with pion sources and sinks of definite spatial momentum[2] $\mathbf{P}$,

$$C_{\rm 3pt}[\hat{O}](t_i,t,t_f,P) \;=\; \sum_{\mathbf{x}_i,\mathbf{x}_f} e^{-i(\mathbf{x}_f-\mathbf{x}_i)\cdot\mathbf{P}} \langle \phi(t_f,\mathbf{x}_f)\hat{O}(t)\phi^\dagger(t_i,\mathbf{x}_i)\rangle \tag{26}$$

$$C_{\rm 2pt}(t_i,t_f,P) \;=\; \sum_{\mathbf{x}_i,\mathbf{x}_f} e^{-i(\mathbf{x}_f-\mathbf{x}_i)\cdot\mathbf{P}} \langle \phi(t_f,\mathbf{x}_f)\phi^\dagger(t_i,\mathbf{x}_i)\rangle \tag{27}$$

where t_i, t and t_f are source time, operator insertion time and sink time, respectively, and ϕ denotes an interpolating field with the quantum numbers of the pion. Wuppertal-smeared quark fields were employed to construct these pion sources and sinks, which were separated by $t_f - t_i = 9a$. Only connected contractions contributing to $C_{\rm 3pt}$ were evaluated; disconnected contributions, which are expected to be small, are omitted in all results presented below. In the case of the π^+ meson, u-quark and $\bar{d}$-quark distributions coincide; contrary to the nucleon case, there is therefore no nontrivial $u-d$ quark combination in which disconnected contributions exactly cancel.

The fundamental correlator (1) is then obtained from plateaus in t for $t_i \ll t \ll t_f$ in the three-point to two-point function ratio [21],

$$\widetilde{\Phi}^{[\Gamma]}_{\rm unsubtr.} = E(P)\frac{C_{\rm 3pt}[\hat{O}](t_i,t,t_f,P)}{C_{\rm 2pt}(t_i,t_f,P)} \tag{28}$$

where $E(P)$ is the energy of the pion state and $\hat{O}$ is taken to be the operator in (1). It should be noted that, at the employed source-sink separation of $t_f - t_i = 9a = 1.07\,\mathrm{fm}$, significant excited state contaminations in the plateaus extracted from (28) cannot be excluded a priori. This issue was not investigated in the present exploratory study at the fairly high pion mass $m_\pi = 518\,\mathrm{MeV}$. However, in future work at lower pion masses, where excited state contaminations are exacerbated, it will present an additional challenge.

The set of combinations of pion momenta and staple-shaped gauge link paths used is listed in Table II. It should be noted that, in the case of either $\mathbf{b}$ or $\mathbf{v}$ extending into a direction which does not coincide with a lattice axis, there is more than one optimal approximation of the corresponding continuum path by a lattice link path; e.g., if $\mathbf{b} = 2(\mathbf{e}_1 + \mathbf{e}_2)$, where $\mathbf{e}_i$ denotes the lattice link vector in i-direction, both the sequence of links $(\mathbf{e}_1,\mathbf{e}_2,\mathbf{e}_1,\mathbf{e}_2)$ and the sequence of links $(\mathbf{e}_2,\mathbf{e}_1,\mathbf{e}_2,\mathbf{e}_1)$ equally well approximate the continuum path. In such a case, $\widetilde{\Phi}^{[\Gamma]}_{\rm unsubtr.}$ was always averaged over all equivalent lattice link paths, for both $\mathbf{b}$ and $\mathbf{v}$ vectors. This symmetry improvement of the lattice operators is important to preserve the manifest time-reversal transformation properties present for the continuum staple-shaped gauge link path operators.

Note also that, in the mixed action scheme used for these calculations, before evaluating domain wall propagators for valence quarks, the asqtad gauge configurations are HYP-smeared to reduce dislocations (or rough fields) that would otherwise allow right-handed states on one domain wall to mix with left-handed states on the other domain wall. The lattice gauge link paths in (1) were constructed using those same HYP-smeared gauge configurations. This has the advantageous consequence that renormalization constants are closer to their tree-level values, while it would have no effect in the continuum limit. Concerning the dependence of the renormalization constants and soft factors on HYP-smearing, it is worth noting the significant differences observed between 0 and 2 steps of HYP-smearing in the direct calculation of parton distributions using straight gauge link paths instead of staples, cf. Figs. 3-5 in ref. [20].

---

[2] In practice, momentum conservation eliminates the need for projection at the source, provided one projects onto zero momentum transfer at the operator insertion in $C_{\rm 3pt}$ instead.

$\mathbf{b}/a$	$\eta\mathbf{v}/a$	$\mathbf{P}\cdot aL/(2\pi)$
$n\cdot(0,0,1), n=-9,\ldots,9$	$\pm n'\cdot(1,0,0)$	$(0,0,0)$, $(-1,0,0)$, $(-2,0,0)$, $(0,-2,0)$, $(-1,-1,0)$, $(-2,-1,0)$
	$\pm n'\cdot(0,1,0)$	$(0,0,0)$, $(-1,0,0)$, $(-2,0,0)$, $(0,-2,0)$, $(-1,-1,0)$, $(-2,-1,0)$
	$\pm n'\cdot(1,1,0)$	$(0,0,0)$, $(-1,0,0)$, $(-2,0,0)$, $(0,-2,0)$, $(-1,-1,0)$, $(-2,-1,0)$
	$\pm n'\cdot(1,-1,0)$	$(0,0,0)$, $(-1,0,0)$, $(-2,0,0)$, $(0,-2,0)$, $(-2,-1,0)$
	$\pm n'\cdot(2,1,0)$	$(-2,-1,0)$
	$\pm n'\cdot(2,-1,0)$	$(-2,-1,0)$
$n\cdot(0,1,0), n=-9,\ldots,9$	$\pm n'\cdot(1,0,0)$	$(0,0,0)$, $(-1,0,0)$, $(-2,0,0)$, $(0,0,-2)$
	$\pm n'\cdot(0,0,1)$	$(0,0,0)$, $(-1,0,0)$, $(-2,0,0)$, $(0,0,-2)$
	$\pm n'\cdot(1,0,1)$	$(0,0,0)$, $(-1,0,0)$, $(-2,0,0)$, $(0,0,-2)$
	$\pm n'\cdot(1,0,-1)$	$(0,0,0)$, $(-1,0,0)$, $(-2,0,0)$, $(0,0,-2)$
$n\cdot(1,0,0), n=-9,\ldots,9$	$\pm n'\cdot(0,1,0)$	$(0,-2,0)$, $(0,0,-2)$
	$\pm n'\cdot(0,0,1)$	$(0,-2,0)$, $(0,0,-2)$
	$\pm n'\cdot(0,1,1)$	$(0,-2,0)$, $(0,0,-2)$
	$\pm n'\cdot(0,1,-1)$	$(0,-2,0)$, $(0,0,-2)$
$n\cdot(0,1,1), n=-4,\ldots,4$	$\pm n'\cdot(1,0,0)$	$(0,0,0)$, $(-1,0,0)$, $(-2,0,0)$
$n\cdot(0,1,-1), n=-4,\ldots,4$	$\pm n'\cdot(1,0,0)$	$(0,0,0)$, $(-1,0,0)$, $(-2,0,0)$, $(-1,-1,-1)$
	$\pm n'\cdot(0,1,1)$	$(-1,-1,-1)$
$n\cdot(1,0,1), n=-4,\ldots,4$	$\pm n'\cdot(0,1,0)$	$(0,-2,0)$
$n\cdot(1,0,-1), n=-4,\ldots,4$	$\pm n'\cdot(0,1,0)$	$(0,-2,0)$, $(-1,-1,-1)$
	$\pm n'\cdot(1,0,1)$	$(-1,-1,-1)$
$n\cdot(1,1,0), n=-4,\ldots,4$	$\pm n'\cdot(0,0,1)$	$(0,0,-2)$
$n\cdot(1,-1,0), n=-4,\ldots,4$	$\pm n'\cdot(0,0,1)$	$(0,0,-2)$, $(-1,-1,0)$, $(-1,-1,-1)$
	$\pm n'\cdot(1,1,0)$	$(-1,-1,0)$, $(-1,-1,-1)$
$n\cdot(0,2,1), n=-3,\ldots,3$	$\pm n'\cdot(1,0,0)$	$(0,0,0)$, $(-1,0,0)$, $(-2,0,0)$
$n\cdot(0,2,-1), n=-3,\ldots,3$	$\pm n'\cdot(1,0,0)$	$(0,0,0)$, $(-1,0,0)$, $(-2,0,0)$
$n\cdot(0,1,2), n=-3,\ldots,3$	$\pm n'\cdot(1,0,0)$	$(0,0,0)$, $(-1,0,0)$, $(-2,0,0)$
$n\cdot(0,1,-2), n=-3,\ldots,3$	$\pm n'\cdot(1,0,0)$	$(0,0,0)$, $(-1,0,0)$, $(-2,0,0)$
$n\cdot(2,0,1), n=-3,\ldots,3$	$\pm n'\cdot(0,1,0)$	$(0,-2,0)$
$n\cdot(2,0,-1), n=-3,\ldots,3$	$\pm n'\cdot(0,1,0)$	$(0,-2,0)$
$n\cdot(1,0,2), n=-3,\ldots,3$	$\pm n'\cdot(0,1,0)$	$(0,-2,0)$
$n\cdot(1,0,-2), n=-3,\ldots,3$	$\pm n'\cdot(0,1,0)$	$(0,-2,0)$
$n\cdot(2,1,0), n=-3,\ldots,3$	$\pm n'\cdot(0,0,1)$	$(0,0,-2)$
$n\cdot(2,-1,0), n=-3,\ldots,3$	$\pm n'\cdot(0,0,1)$	$(0,0,-2)$
$n\cdot(1,2,0), n=-3,\ldots,3$	$\pm n'\cdot(0,0,1)$	$(0,0,-2)$
$n\cdot(1,-2,0), n=-3,\ldots,3$	$\pm n'\cdot(0,0,1)$	$(0,0,-2)$, $(-2,-1,0)$
	$\pm n'\cdot(2,1,0)$	$(-2,-1,0)$

TABLE II: Sets of staple-shaped gauge link paths and spatial pion momenta $\mathbf{P}$ used on the lattice. Gauge link paths are characterized by the quark separation vector $\mathbf{b}$ and the staple vector $\eta\mathbf{v}$, cf. Fig. 1. The surveyed range of η, parameterized in the table by the integer n', was always chosen to extend from zero to well beyond the point where a numerical signal ceases to be discernible. The maximal magnitude of the Collins-Soper parameter $\hat{\zeta}$ attained in these sets is $|\hat{\zeta}| = 2.03$, for $\mathbf{P}\cdot aL/(2\pi) = (-2,0,0)$ paired with $\eta\mathbf{v}/a = \pm n'\cdot(1,0,0)$ and rotations thereof.

The optimal use of HYP-smearing thus deserves further study. It should again be emphasized, however, that the ratio observables studied in the framework employed here are designed to cancel renormalization constants and soft factors, and therefore the results are expected to be essentially independent of HYP-smearing, apart from data at small separations, at which discretization artefacts presumably are alleviated. Dedicated studies of the dependence of the TMD observables considered here on the lattice discretization are the subject of ongoing work [52].

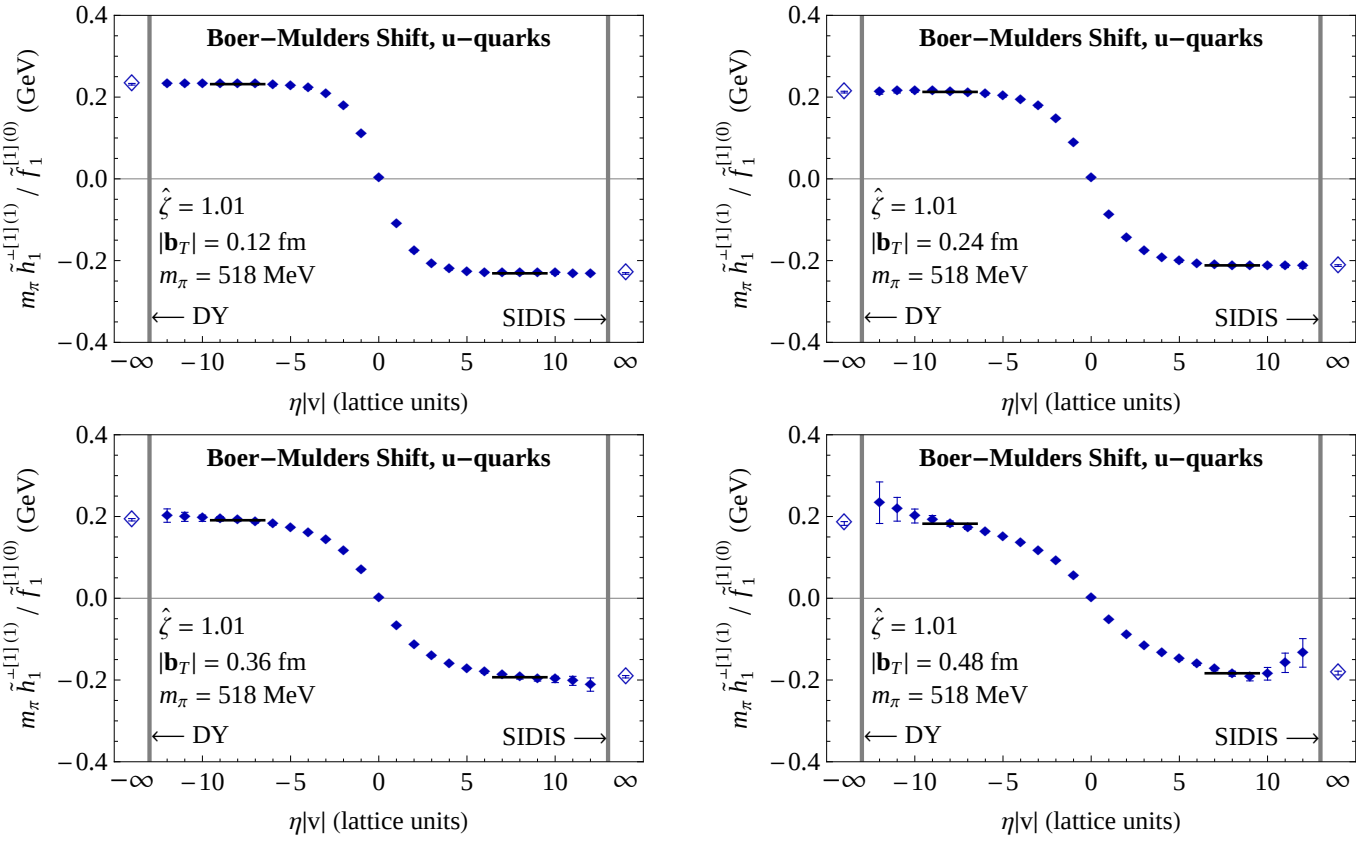

FIG. 2: Generalized Boer-Mulders shift for u-quarks as a function of staple extent $\eta|v|$, for fixed $\hat{\zeta} = 1.01$; the panels illustrate data obtained at a succession of quark separations $|b_T|$. Plateau fits and extraction of asymptotic values (open symbols) are described in the main text.

IV. NUMERICAL RESULTS

A. SIDIS and DY limits

The first step in the analysis of the obtained data concerns the behavior as a function of staple length η. For ease of notation, both positive and negative η are considered for a fixed $v \cdot P > 0$ to distinguish staples oriented in the forward and backward directions with respect to the pion momentum. Of particular physical interest is the asymptotic behavior for $\eta \to \pm\infty$, corresponding to the SIDIS and DY limits. Fig. 2 displays results for the u-quark generalized Boer-Mulders shift as a function of $\eta|v|$ at a fixed $\hat{\zeta} = 1.01$, with each of the four panels corresponding to a successively larger transverse quark separation $|b_T|$. The T-odd behavior of the observable is evident. As the SIDIS and DY limits are approached, a clear plateau behavior in $\eta|v|$ is observed up to moderate values of $|b_T|$; as $|b_T|$ rises, statistical uncertainties increase (as indicated by the jackknife error estimates in the plots), and the identification of the plateaus becomes more tenuous, cf., e.g., the lower right panel, for $|b_T| = 0.48\,\mathrm{fm}$. Plateau values are extracted by averaging over the regions $7a \le \eta|v| \le 9a$ and $-7a \ge \eta|v| \ge -9a$, respectively, as indicated by the fit lines in the plots; this appeared to constitute the best compromise between systematic bias at at low $|\eta v|$ and statistical fluctuations at high $|\eta v|$. Finally, the SIDIS and DY limits are obtained imposing T-oddness, i.e., the two plateau values in each plot are averaged with a relative minus sign to yield the asymptotic SIDIS and DY estimates also displayed in the panels (open symbols). The asymptotic values slightly decrease in magnitude as $|b_T|$ rises.

Fig. 3 summarizes the results obtained in the SIDIS limit as a function of the quark separation $|b_T|$, for three different values of the Collins-Soper parameter $\hat{\zeta}$. Note that the data at small $|b_T|$, up to $|b_T| \approx 2a = 0.24\,\mathrm{fm}$, may be affected by discretization artefacts, but at larger $|b_T|$, the data are expected to well approximate the continuum limit. For larger $\hat{\zeta}$, cf. also further examples below, the statistical fluctuations rapidly increase, and no useful signal was obtained beyond $|b_T| = 0.5\,\mathrm{fm}$ in the case $\hat{\zeta} = 2.03$. The data appear to approach well-defined limits as either $|b_T|$ or $\hat{\zeta}$ becomes large. The behavior as a function of $\hat{\zeta}$ will be discussed in greater detail below; the behavior as $|b_T|$ becomes

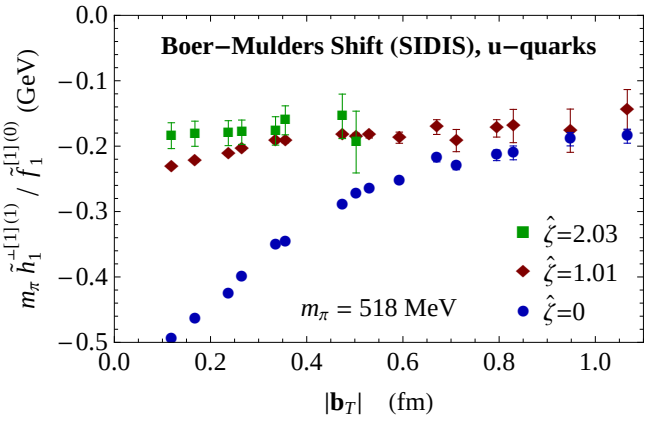

FIG. 3: Generalized Boer-Mulders shift for u-quarks in the SIDIS limit as a function of the quark separation $|b_T|$, for three different values of the Collins-Soper parameter $\hat{\zeta}$. The shown uncertainties are statistical jackknife errors.

large seems plausible: Physically, once $|b_T|$ exceeds the size of the pion, the correlator (1) cannot anymore probe correlations inside the pion; it only contains vacuum-vacuum and vacuum-pion correlations. The $|b_T|$-dependence of these correlations is then expected to be dominated by the typical exponential fall-off with $|b_T|$ observed in the vacuum[3]; neglecting all other dependences in comparison, and canceling the dominant behavior in the ratio (23) leads to the expectation of a constant asymptotic behavior in $|b_T|$.

As $\hat{\zeta}$ increases, one furthermore would expect the aforementioned constant to converge to an asymptotic limit. Remarkably, however, even the $\hat{\zeta} = 0$ data appear to already approach the same large-$|b_T|$ constant as the data at higher $\hat{\zeta}$. Possibly, this may be understood as a consequence of the Lorentz invariance of the vacuum; only vacuum-vacuum and vacuum-pion correlations are probed at large $|b_T|$, and it seems plausible that these would be independent of the pion momentum. It would be desirable to gain a more definite understanding of this property. The most remarkable feature of the data, however, is the apparent tendency of the generalized Boer-Mulders shift to become constant in $|b_T|$ as $\hat{\zeta}$ is increased, not only for asymptotic values of $|b_T|$, but for all $|b_T|$. No obvious reason for this behavior at low to intermediate $|b_T|$ is apparent, and it would be very interesting to develop an understanding of it. The constant behavior implies that, in the relevant transverse momentum $|k_T|$ range corresponding to the probed range of $|b_T|$, the transverse momentum spectrum of polarized quarks is the same as for unpolarized ones.

B. Evolution in $\hat{\zeta}$

A special focus of the present investigation is the behavior as a function of $\hat{\zeta}$ and the large $\hat{\zeta}$ limit, i.e., studying in detail the behavior of the sequence of data seen in Fig. 3 at a fixed value of $|b_T|$. Fig. 4 shows two further panels analogous to the ones in Fig. 2, but with $\hat{\zeta}$ varying between the panels and $|b_T| = 0.36\,\text{fm}$ fixed instead. Thus, in terms of a $\hat{\zeta}$ sequence, the lower left panel of Fig. 2 lies in between the two panels displayed in Fig. 4. As already mentioned further above, for pion spatial momentum $\mathbf{P} = 0$, corresponding to the left panel in Fig. 4, there is only one branch as a function of $\eta|v|$, as shown. The right panel in Fig. 4, corresponding to $\hat{\zeta} = 2.03$, illustrates the rapid deterioration of signal as the pion momentum is increased. Nevertheless, at the moderate $|b_T|$ used here, a plateau can still be extracted.

Fig. 5 summarizes all results obtained in the SIDIS limit at $|b_T| = 0.36\,\text{fm}$ as a function of the Collins-Soper

[3] Heuristically, the expectation value of the gauge link staple, which, after integrating out the quark fields, may be thought of as being completed into a closed loop by the (fluctuating) world lines of dynamically propagating quarks, is expected to be determined by the chromodynamic flux piercing the loop. This is, e.g., the origin of the Wilson loop area law demonstrating confinement in Yang-Mills theory [53]. Once $|b_T|$ exceeds the size of the pion, at most one of the legs of the staple can traverse the pion; the other runs entirely within the vacuum. Consider now varying $|b_T|$ by shifting the latter leg; the area being added or removed from the loop lies purely within the vacuum. Only vacuum chromodynamic flux is being added or subtracted, while the chromodynamic flux influenced by the pion remains fixed. Thus, the variation of the expectation value with $|b_T|$ is determined purely by vacuum properties (which is not to say that the expectation value becomes entirely independent of the properties of the pion; only its $|b_T|$-dependence does). This argument is unchanged if one subsequently averages over different positions of the leg of the staple traversing the pion.

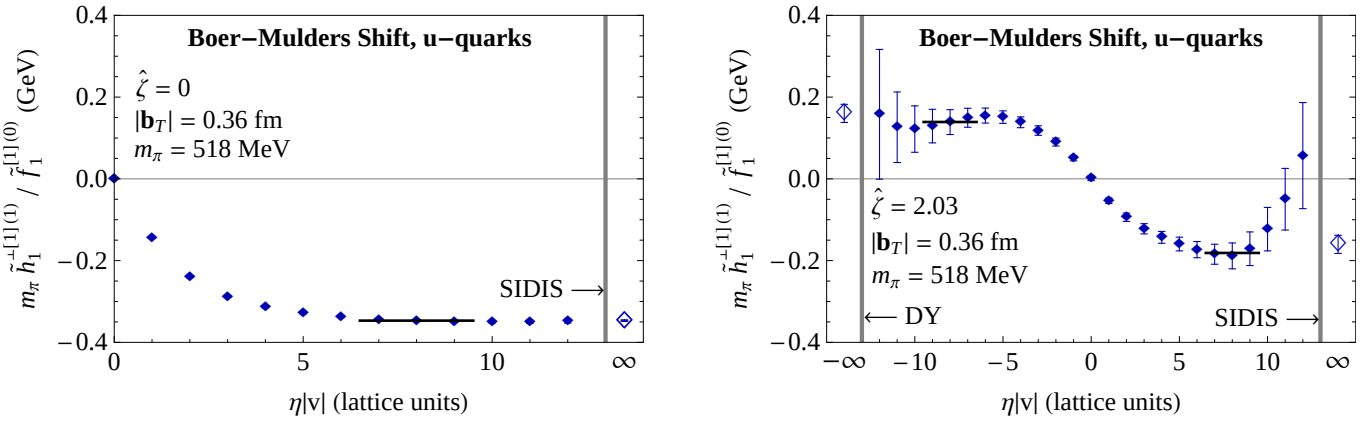

FIG. 4: Generalized Boer-Mulders shift for u-quarks as a function of staple extent $\eta|v|$, analogous to Fig. 2, but at fixed $|b_T| = 0.36\,\mathrm{fm}$ and $\hat{\zeta}$ varying between the panels instead. In terms of a $\hat{\zeta}$ sequence, the lower left panel of Fig. 2 lies in between the two panels shown here. For pion spatial momentum $\mathbf{P} = 0$ (left panel), there is only one branch as a function of $\eta|v|$.

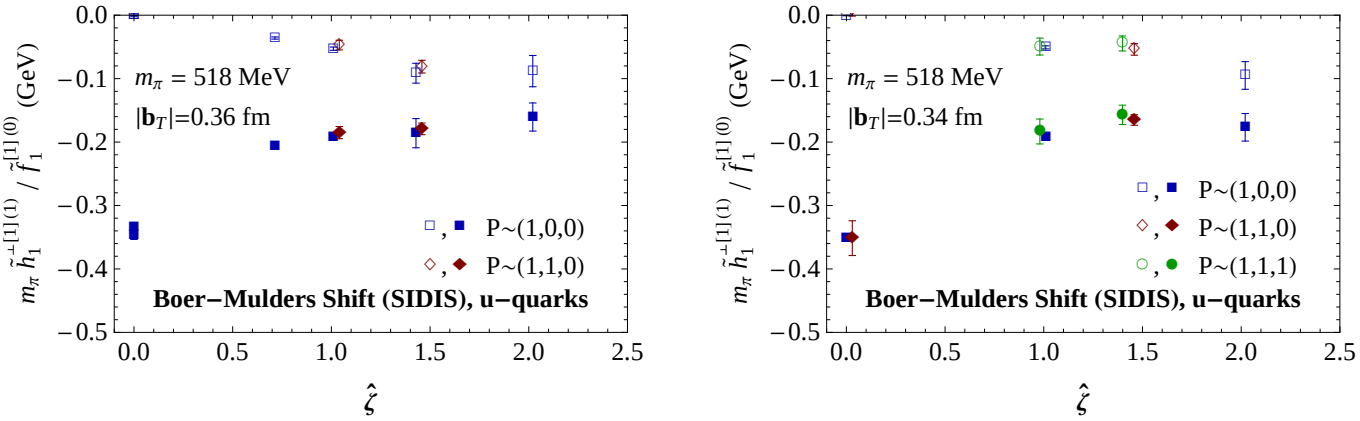

FIG. 5: Generalized Boer-Mulders shift for u-quarks in the SIDIS limit as a function of the Collins-Soper parameter $\hat{\zeta}$, for fixed quark separation $|b_T| = 0.36\,\mathrm{fm}$ (left) and $|b_T| = 0.34\,\mathrm{fm}$ (right). Filled symbols correspond to the full generalized Boer-Mulders shift, whereas open symbols correspond to the partial contribution obtained by replacing $\widetilde{A}_{4B}$ in (23) by $\widetilde{A}_4$, for further discussion, cf. main text. Spatial pion momenta $\mathbf{P}$ along various directions, as labeled, were employed; labels in general subsume more than one magnitude along the specified axis, cf. Table II for the complete set of momenta for which data were generated. Data labeled $\mathbf{P} \sim (1,0,0)$ include averaging over 90 degree rotations thereof, i.e., momenta along any of the three spatial lattice axes are included. A given value of $\hat{\zeta}$ can be accessed using different pairs of $\mathbf{P}$ and staple direction v; in such cases, data corresponding to different $\mathbf{P}$ directions are slightly offset from one another horizontally for better visibility. The shown uncertainties are statistical jackknife errors.

parameter $\hat{\zeta}$ (left panel), and analogous data for the nearby value $|b_T| = 0.34\,\mathrm{fm}$ (right panel). From the figure, the good rotational properties of the calculation are evident; a given value of $\hat{\zeta}$ can be accessed using different directions of the pion spatial momentum $\mathbf{P}$ and the staple direction v, including both on- and off-axis directions, as shown. The corresponding results coincide, indicating that potential lattice artefacts are under control, and thus buttressing the physical significance of the data obtained. To assess the asymptotic behavior at large $\hat{\zeta}$, it is advantageous to consider not only the full generalized Boer-Mulders shift, but also the partial contribution obtained by replacing $\widetilde{A}_{4B}$ in (23) by $\widetilde{A}_4$, omitting the contribution from $\widetilde{B}_3$, cf. eq. (18). Both quantities are displayed Fig. 5; as is evident from the figure, the partial $\widetilde{A}_4$ contribution vanishes at $\hat{\zeta} = 0$, but monotonically increases in magnitude as $\hat{\zeta}$ is increased. By contrast, the remaining contribution from $\widetilde{B}_3$ to the full generalized Boer-Mulders shift, dominant at $\hat{\zeta} = 0$, decreases in magnitude as $\hat{\zeta}$ rises. This matches the behavior expected from eq. (18), according to which the contribution from $\widetilde{B}_3$ becomes insignificant for $\hat{\zeta} \to \infty$ under the assumption that the amplitude $\widetilde{B}_3$ stays finite. Altogether, the full generalized Boer-Mulders shift also decreases in magnitude as $\hat{\zeta}$ increases. Thus, the behavior of the data suggests that, by considering both quantities, one has access to both lower and upper bounds for the generalized Boer-Mulders

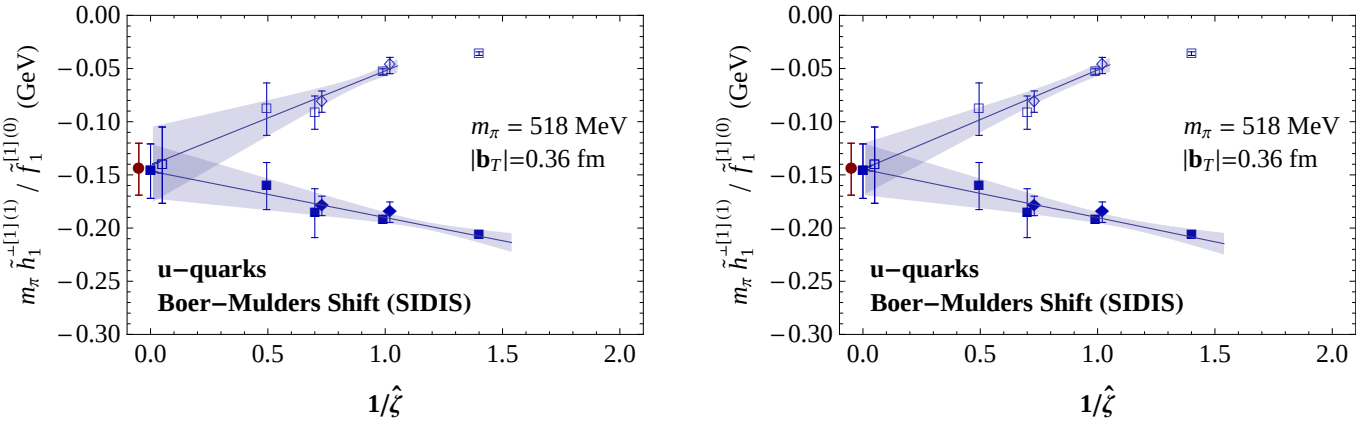

FIG. 6: Least-squares fits to generalized Boer-Mulders shift data shown in Fig. 5 (left), excluding $\hat{\zeta} = 0$ points, using fit ansatz $c + d/\hat{\zeta}$. Left panel displays separate fits to filled and open data points; right panel displays combined fit, cf. main text. Error bands show statistical jackknife uncertainties of the fits. In the case of the open symbols, the data point at highest $1/\hat{\zeta}$ was not taken into account in the fits, because it already lies in the region of an apparent inflection point, cf. Fig. 5 (left), at which the simple asymptotic fit ansatz certainly is not applicable anymore. Data points at $1/\hat{\zeta} = 0$ represent the extrapolated values. For easier comparison, both panels show all three asymptotic data, slightly separated horizontally for better visibility: The separate fits to the filled and open data points (filled and open squares), as well as the result of the combined fit (filled circle). The shown uncertainties are statistical jackknife errors.

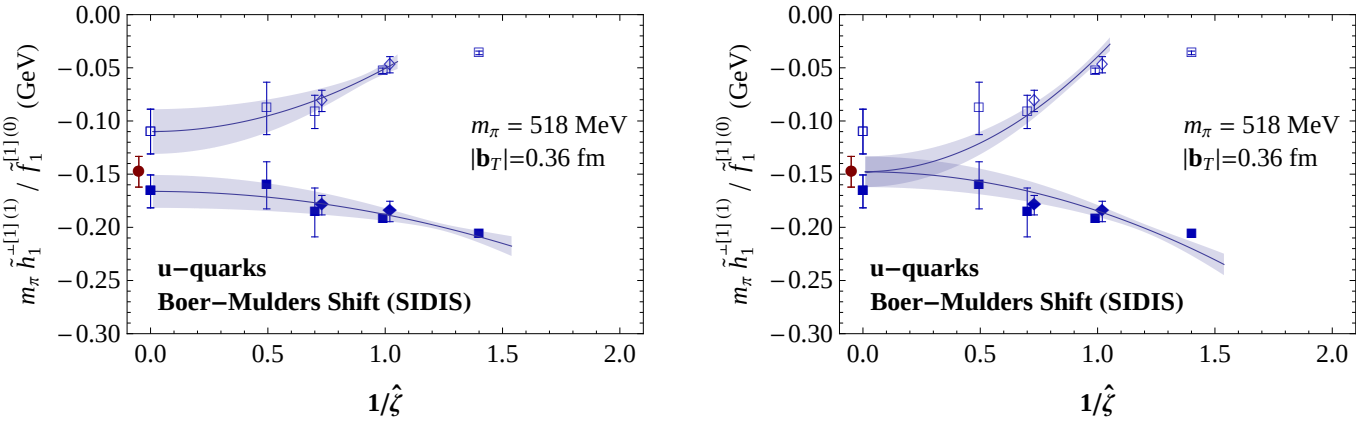

FIG. 7: Least-squares fits to generalized Boer-Mulders shift data shown in Fig. 5 (left), analogous to Fig. 6, except using fit ansatz $c + d/\hat{\zeta}^2$.

shift, considerably increasing the confidence in the extrapolations to large $\hat{\zeta}$ discussed below. The comparison between the partial and full quantities also permits an assessment of the extent to which evolution in $\hat{\zeta}$ has progressed towards the asymptotic limit. Evidently, according to Fig. 5, already about half of the magnitude of the full generalized Boer-Mulders shift is subsumed in the partial $\widetilde{A}_4$ contribution at $\hat{\zeta} \approx 2$. A significant part of the $\hat{\zeta}$ evolution has thus already been achieved at that value of $\hat{\zeta}$. In this respect, the present study yields a much clearer picture than was obtained in the previous nucleon investigation [13].

To obtain quantitative statements about the large $\hat{\zeta}$ limit, least-squares fits[4] to the $\hat{\zeta}$-dependences of the data were performed, using power-correction ansätze of the form $c + d/\hat{\zeta}$ and $c + d/\hat{\zeta}^2$. It should be noted that the values of $\hat{\zeta}$ for which data were obtained in the present study do not reach clearly into the perturbative regime within which a reliable connection to perturbative evolution can be guaranteed. The aforementioned fit functions should therefore be

[4] Whereas the data at higher $\hat{\zeta}$ generally display the larger statistical uncertainties, the data at lower $\hat{\zeta}$ are likely to deviate systematically to a larger degree from any putative simple asymptotic behavior. It therefore does not seem appropriate to bias the fits towards the lower $\hat{\zeta}$ data by performing a χ^2 fit taking into account the statistical uncertainties.

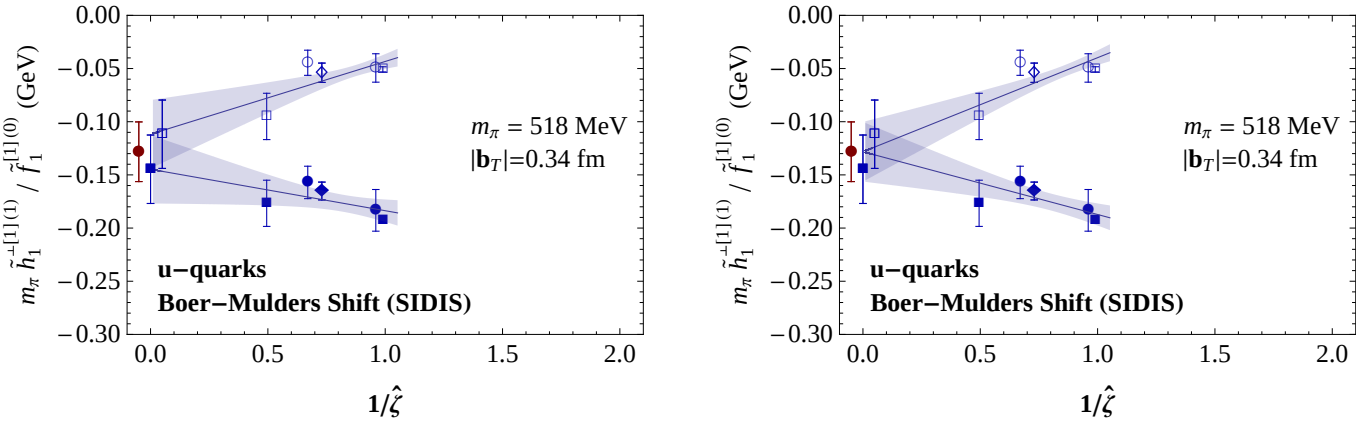

FIG. 8: Least-squares fits to generalized Boer-Mulders shift data shown in Fig. 5 (right), excluding $\hat{\zeta} = 0$ points, using fit ansatz $c + d/\hat{\zeta}$. Left panel displays separate fits to filled and open data points; right panel displays combined fit, cf. main text. Error bands show statistical jackknife uncertainties of the fits. Data points at $1/\hat{\zeta} = 0$ represent the extrapolated values. For easier comparison, both panels show all three asymptotic data, slightly separated horizontally for better visibility: The separate fits to the filled and open data points (filled and open squares), as well as the result of the combined fit (filled circle). The shown uncertainties are statistical jackknife errors.

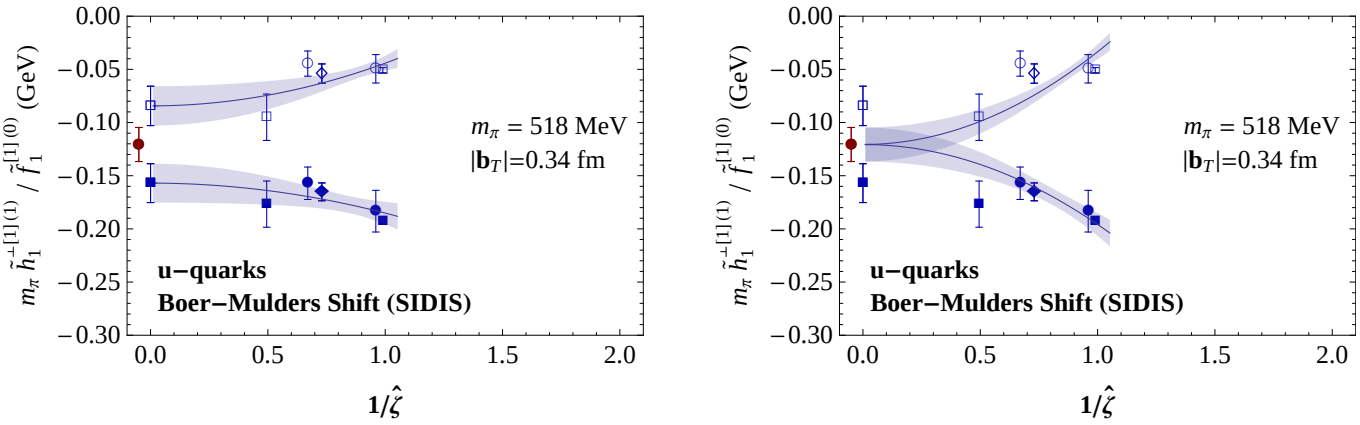

FIG. 9: Least-squares fits to generalized Boer-Mulders shift data shown in Fig. 5 (right), analogous to Fig. 8, except using fit ansatz $c + d/\hat{\zeta}^2$.

regarded as ad hoc ansätze. On the one hand, separate fits to the full generalized Boer-Mulders shift data and to the partial $\widetilde{A}_4$ contribution were performed; on the other hand, a combined fit to both quantities with a common constant c (but, of course, separate coefficients d) was carried out. The results are shown in Figs. 6-11, and the asymptotic values summarized in Table III. Figs. 6 and 7 display the fits to the data of Fig. 5 (left), at $|b_T| = 0.36\,\text{fm}$, whereas Figs. 8 and 9 display the fits to the data of Fig. 5 (right), at $|b_T| = 0.34\,\text{fm}$. Figs. 10 and 11 additionally display fits to data obtained at a lower $|b_T|$, namely, $|b_T| = 0.27\,\text{fm}$.

The fits using the form $c + d/\hat{\zeta}$ are superior to those using the form $c + d/\hat{\zeta}^2$. In the former case, the asymptotic values obtained by analyzing the full generalized Boer-Mulders shift data and the partial $\widetilde{A}_4$ contribution separately agree within uncertainties, and also with the result of the combined fit. In the latter case, the asymptotic values obtained with the separate fits differ significantly. Not surprisingly, the results of the combined fits using the two fit ansätze are quite similar; by construction, they settle roughly in the middle between the two separate quantities. Nevertheless, also in the combined fits, the $c + d/\hat{\zeta}$ ansatz is more favorable, as evidenced by the last column in Table III, which gives the root mean square deviation, per degree of freedom, of the combined fit from the data means. The deviation is considerably larger for the $c + d/\hat{\zeta}^2$ fits; it is of the order of, or larger than, the jackknife statistical uncertainty of the asymptotic value. By contrast, for the $c + d/\hat{\zeta}$ ansatz, the deviation is considerably smaller than the jackknife statistical uncertainty of the asymptotic value. These observations favor the $c + d/\hat{\zeta}$ fit ansatz.

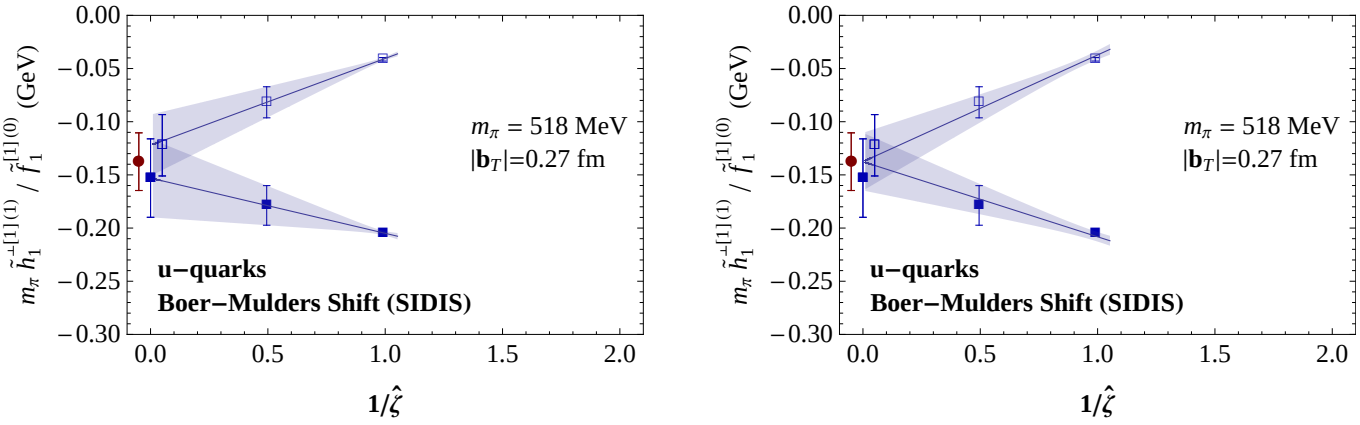

FIG. 10: Least-squares fits to generalized Boer-Mulders shift data at $|b_T| = 0.27\,\mathrm{fm}$, analogous to Figs. 6-9, using fit ansatz $c + d/\hat{\zeta}$. The data were all obtained using spatial pion momenta $\mathbf{P}$ along the lattice axes ($\mathbf{P} \sim (1,0,0)$ in the nomenclature of Fig. 5, including multiples and 90 degree rotations thereof, cf. Table II for the complete set of momenta for which data were generated). Left panel displays separate fits to filled and open data points; right panel displays combined fit, cf. main text. Error bands show statistical jackknife uncertainties of the fits. Data points at $1/\hat{\zeta} = 0$ represent the extrapolated values. For easier comparison, both panels show all three asymptotic data, slightly separated horizontally for better visibility: The separate fits to the filled and open data points (filled and open squares), as well as the result of the combined fit (filled circle). The shown uncertainties are statistical jackknife errors.

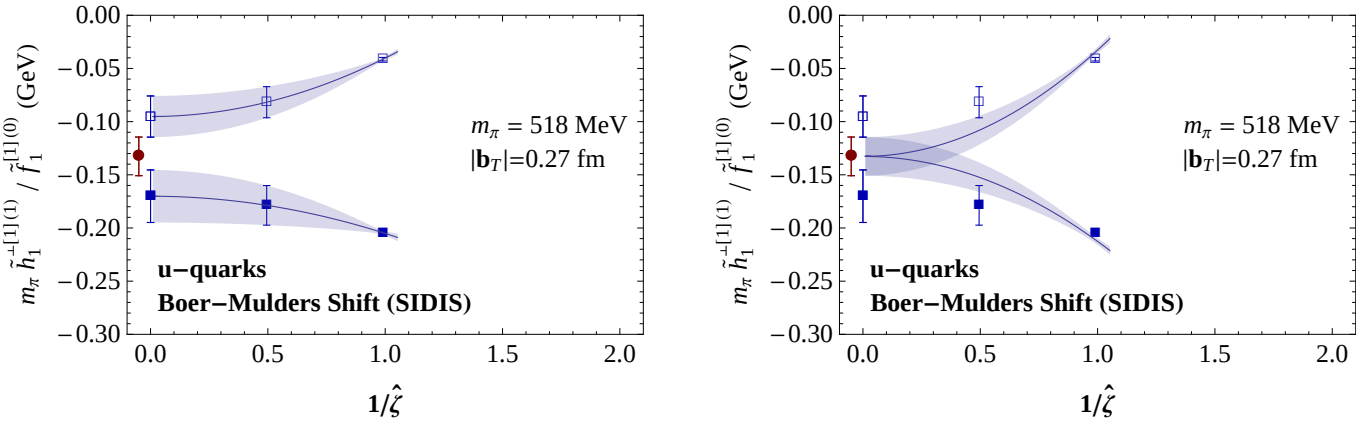

FIG. 11: Least-squares fits to generalized Boer-Mulders shift data at $|b_T| = 0.27\,\mathrm{fm}$, analogous to Fig. 10, except using fit ansatz $c + d/\hat{\zeta}^2$.

	Fit function	Full B.-M. shift (GeV)	Contribution $\widetilde{A}_4$ only (GeV)	Combined fit (GeV)	RMS deviation of combined fit (GeV)
$\|b_T\| = 0.36\,\mathrm{fm}$	$c + d/\hat{\zeta}$	-0.146(26)	-0.141(36)	-0.145(25)	0.00755
$\|b_T\| = 0.36\,\mathrm{fm}$	$c + d/\hat{\zeta}^2$	-0.166(16)	-0.110(22)	-0.148(15)	0.01695
$\|b_T\| = 0.34\,\mathrm{fm}$	$c + d/\hat{\zeta}$	-0.145(33)	-0.112(33)	-0.128(29)	0.01466
$\|b_T\| = 0.34\,\mathrm{fm}$	$c + d/\hat{\zeta}^2$	-0.157(19)	-0.084(19)	-0.121(16)	0.02315
$\|b_T\| = 0.27\,\mathrm{fm}$	$c + d/\hat{\zeta}$	-0.153(37)	-0.122(29)	-0.138(28)	0.00975
$\|b_T\| = 0.27\,\mathrm{fm}$	$c + d/\hat{\zeta}^2$	-0.170(25)	-0.095(20)	-0.133(19)	0.03855

TABLE III: Asymptotic values of least-squares fits to the $\hat{\zeta}$-dependences of the full generalized Boer-Mulders shift and the partial $\widetilde{A}_4$ contribution separately, as well as a combined fit. These are the values displayed at $1/\hat{\zeta} = 0$ in Figs. 6-11. Uncertainties quoted are statistical jackknife errors. The right-hand column gives the root mean square deviation, per degree of freedom, of the combined fit from the data means.

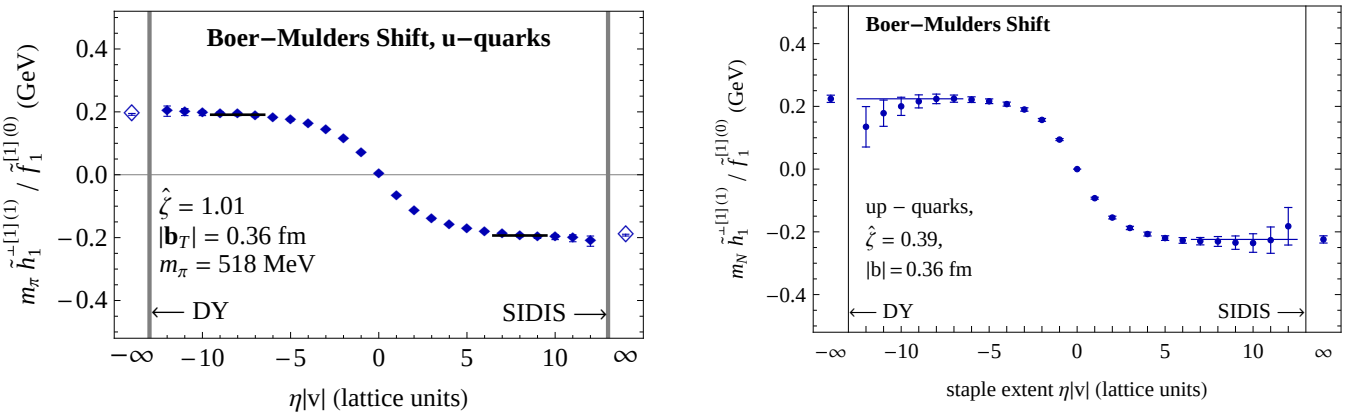

FIG. 12: Generalized Boer-Mulders shift for u-quarks in a π^+-meson (left) and a proton [13] (right), as a function of staple extent $\eta|v|$, for quark separation $|b_T| = 0.36\,\mathrm{fm}$. The data in the two panels were obtained using the same spatial hadron momentum $\mathbf{P}$ and staple direction v. This corresponds to identical $\zeta = 2m_h\hat{\zeta}$, but, consequently, differing $\hat{\zeta}$, as labeled in the panels, cf. main text for further discussion. Plateau fits and extraction of asymptotic values are analogous to Fig. 2. In the proton case, taken from the analysis described in [13], a wider fit range was used.

Note that the asymptotic values for the generalized Boer-Mulders shift obtained using the $c + d/\hat{\zeta}$ ansatz both at $|b_T| = 0.36\,\mathrm{fm}$ and at $|b_T| = 0.34\,\mathrm{fm}$, as well as at the lower separation $|b_T| = 0.27\,\mathrm{fm}$, all coincide within uncertainties. These extrapolations thus do not modify the observation made further above in connection with Fig. 3, namely, that the generalized Boer-Mulders shift appears to become constant in $|b_T|$ as $\hat{\zeta}$ becomes large.

Altogether, it is encouraging to observe that the data generated in the present study are of sufficient quality to ensure that the signal survives extrapolation to the $\hat{\zeta} \to \infty$ limit, with an uncertainty as low as, roughly, 20% for the selected parameter values analyzed above. It is possible to tentatively discriminate between different asymptotic models. Further improvements of the analysis are to be expected by confronting lattice data with perturbative evolution equations for the observables considered here; at present, perturbative QCD predictions for the asymptotic behavior of the generalized Boer-Mulders shift are not available.

C. Pion-proton comparison

In [54], the question was posed how similar Boer-Mulders functions are in different hadrons, and also for different flavors. The present study permits addressing this question in passing, since Boer-Mulders data are now available on the same lattice ensemble both for nucleons [13] and for pions, obtained here, with corresponding parameters, facilitating a comparison. Fig. 12 provides a sample juxtaposition of the π^+-meson and proton u-quark generalized Boer-Mulders shifts generated on the same ensemble, at identical transverse quark separation $|b_T| = 0.36\,\mathrm{fm}$, and identical spatial hadron momentum $\mathbf{P}$ and staple direction v, as a function of staple extent. This corresponds to identical $\zeta = 2m_h\hat{\zeta}$, but of course $\hat{\zeta}$ then differs because of the appearance of the hadron mass in the denominator of (4). In this particular juxtaposition, the behavior of the two shifts is seen to be very similar. In the proton, the approach to the large $|\eta|$ plateaus appears to be slightly faster; the plateaus lie within 10% of one another. One could argue that the more appropriate comparison is one at identical $\hat{\zeta}$, and not at identical ζ, as shown here. However, using identical $\hat{\zeta}$ makes the correspondence hardly less favorable. If one interpolates the SIDIS limit pion data at $|b_T| = 0.36\,\mathrm{fm}$ shown in Fig. 5 (left) from $\hat{\zeta} = 1.01$ to $\hat{\zeta} = 0.39$, the $\hat{\zeta}$ value corresponding to the proton data in Fig. 12 (right), then the pion data are enhanced in magnitude by around 20%, rendering the pion data about 10% higher in magnitude than the proton data, as opposed to 10% lower in the comparison at equal ζ.

Of course, it should be noted that a close quantitative correspondence to the degree observed here for the u-quark generalized Boer-Mulders shifts is not generic. In the π^+-meson, the $\bar{d}$-quark Boer-Mulders shift is identical to the u-quark one, whereas in the proton, the d-quark Boer-Mulders shift is appreciably higher in magnitude compared to the u-quark one [13]. The corresponding comparison would therefore not reveal a similarly close quantitative agreement. Nevertheless, qualitative features such as the signs of the different flavor contributions remain in correspondence.

V. SUMMARY AND OUTLOOK

Building on the previous study [13] of transverse momentum-dependent parton distributions in the nucleon, the present work focused in particular on the evolution of TMD ratios such as the generalized Boer-Mulders shift (23) as a function of the Collins-Soper parameter $\hat{\zeta}$, cf. (4). To this end, the behavior of this TMD observable in a pion was explored; the pion, by virtue of its lower mass, allows one to access higher $\hat{\zeta}$, and the spinless nature of the pion facilitates spatial averaging to increase statistics. Indeed, in contrast to the nucleon study [13], which did not yield definite conclusions concerning the large-$\hat{\zeta}$ limit, the present investigation provides data of sufficient quality to perform tentative extrapolations to $\hat{\zeta} = \infty$. While it is presently not possible to match the generated data to perturbative evolution equations in $\hat{\zeta}$, the ad hoc extrapolations explored here lead to estimates of the $\hat{\zeta} = \infty$ limit of the generalized Boer-Mulders shift (23) to within an uncertainty of as low as roughly 20%, for favorable values of the transverse quark separation b_T, cf. Table III. The confidence in these extrapolations is buttressed in particular by the ability to partition the generalized Boer-Mulders shift into two separate contributions, as discussed in detail in section IV B, such that one is provided with both an upper and a lower bound for the asymptotic behavior.

Having obtained data for the generalized Boer-Mulders shift in the pion, the present study, together with [13], in passing also permits a juxtaposition of pion and nucleon TMD observables. A close correspondence between the u-quark generalized Boer-Mulders shifts in a π^+-meson and a proton is observed, corroborating the behavior conjectured in [24, 54].

Going forward, the success in determining the characteristics of the $\hat{\zeta}$ evolution of the generalized Boer-Mulders shift in a pion suggests that analogous results will also be accessible for nucleons in future lattice studies with higher statistics, focused on obtaining signals at higher nucleon momenta. To this end, it will be useful to explore schemes of generating nucleon interpolating fields with a favorable overlap with higher momentum states. Further efforts currently in progress are concerned with the universality of TMD ratios of the type considered here under variation of the lattice discretization scheme; this is expected to provide empirical support for the working assumption employed here, that the lattice TMD operators are regularized and renormalized in analogy to the corresponding continuum operators, by multiplicative soft factors which cancel in TMD ratios. Moreover, lattice TMD calculations are in progress at lighter pion masses, with a view to transferring the exploratory results obtained here to the physical light quark mass regime.

Acknowledgments

This work benefited from fruitful discussions with T. Bhattacharya, D. Boer, V. Braun, M. Diehl, R. Edwards, R. Gupta, X. Ji, V. Papavassiliou, S. Pate, A. Prokudin, J. Qiu, T. Rogers, X. Wang, B. Yoon and J. Zhang. The lattice calculations performed in this work relied on the Chroma software suite [55] and employed computing resources provided by the U.S. DOE Office of Science through the National Energy Research Scientific Computing Center (NERSC), a DOE Office of Science User Facility, under Contract No. DE-AC02-05CH11231, as well as through facilities of the USQCD Collaboration. Support by the Heisenberg-Fellowship program of the DFG (P.H.), SFB/TRR-55 and the Alexander von Humboldt-Stiftung (A.S.), as well as by the U.S. DOE through grants DE-FG02-96ER40965 (M.E.) and DE-FG02-94ER40818 (J.N.), and through contract DE-AC05-06OR23177, under which Jefferson Science Associates, LLC, operates Jefferson Laboratory (B.M.), is acknowledged.

[1] D. Boer, M. Diehl, R. Milner, R. Venugopalan, W. Vogelsang, D. Kaplan, H. Montgomery, S. Vigdor *et al.*, arXiv:1108.1713.
[2] J. C. Collins, Phys. Lett. **B536**, 43 (2002).
[3] M. Alekseev *et al.* [COMPASS Collaboration], Phys. Lett. **B673**, 127 (2009);
C. Adolph *et al.* [COMPASS Collaboration], Phys. Lett. **B736**, 124 (2014).
[4] A. Airapetian *et al.* [HERMES Collaboration], Phys. Rev. Lett. **103**, 152002 (2009);
A. Airapetian *et al.* [HERMES Collaboration], Phys. Lett. **B728**, 183 (2014).
[5] X. Qian *et al.* [Jefferson Lab Hall A Collaboration], Phys. Rev. Lett. **107**, 072003 (2011);
H. Avakian *et al.* [The CLAS Collaboration], Phys. Rev. Lett. **105**, 262002 (2010).
[6] F. Gautheron *et al.* [COMPASS Collaboration], CERN-SPSC-2010-014 (2010).
[7] C. Brown, D. Geesaman, P. Reimer, D. Christian, M. Diefenthaler *et al.*, FERMILAB-PROPOSAL-1039 (2014).
[8] M. G. Echevarría, A. Idilbi, Z.-B. Kang and I. Vitev, Int. J. Mod. Phys. Conf. Ser. **37**, 1560025 (2015).
[9] A. Adare *et al.* [PHENIX Collaboration], Phys. Rev. **D 90**, 012006 (2014);
L. Adamczyk *et al.* [STAR Collaboration], Phys. Rev. **D 86**, 051101 (2012).

[10] A. Accardi *et al.*, arXiv:1212.1701v3.
[11] P. Hägler, B. U. Musch, J. W. Negele and A. Schäfer, Europhys. Lett. **88**, 61001 (2009).
[12] B. U. Musch, P. Hägler, J. W. Negele and A. Schäfer, Phys. Rev. **D 83**, 094507 (2011).
[13] B. U. Musch, P. Hägler, M. Engelhardt, J. W. Negele and A. Schäfer, Phys. Rev. **D 85**, 094510 (2012).
[14] J. C. Collins, *Foundations of Perturbative QCD* (Cambridge University Press, 2011).
[15] W. Detmold and C. J. D. Lin, Phys. Rev. **D 73**, 014501 (2006).
[16] V. Braun and D. Müller, Eur. Phys. J. **C 55**, 349 (2008).
[17] X. Ji, Phys. Rev. Lett. **110**, 262002 (2013).
[18] H.-W. Lin, J.-W. Chen, S. D. Cohen and X. Ji, Phys. Rev. **D 91**, 054510 (2015).
[19] X. Ji, P. Sun, X. Xiong and F. Yuan, Phys. Rev. **D 91**, 074009 (2015).
[20] C. Alexandrou, K. Cichy, V. Drach, E. Garcia-Ramos, K. Hadjiyiannakou, K. Jansen, F. Steffens and C. Wiese, Phys. Rev. **D 92**, 014502 (2015).
[21] F. Bonnet, R. Edwards, G. Fleming, R. Lewis and D. Richards (LHP Collaboration), Phys. Rev. **D 72**, 054506 (2005).
[22] S. Capitani, C. Gattringer and C. B. Lang, Phys. Rev. **D 73**, 034505 (2006).
[23] D. Brömmel, M. Diehl, M. Göckeler, P. Hägler, R. Horsley, Y. Nakamura, D. Pleiter, P. E. L. Rakow, A. Schäfer, G. Schierholz, H. Stüben and J. M. Zanotti, Eur. Phys. J. **C 51**, 335 (2007).
[24] D. Brömmel *et al.* [QCDSF and UKQCD Collaborations], Phys. Rev. Lett. **101**, 122001 (2008).
[25] J. N. Hedditch, W. Kamleh, B. G. Lasscock, D. B. Leinweber, A. G. Williams and J. M. Zanotti, Phys. Rev. **D 75**, 094504 (2007).
[26] R. Frezzotti, V. Lubicz and S. Simula, Phys. Rev. **D 79**, 074506 (2009).
[27] S. Aoki, T. W. Chiu, H. Fukaya, S. Hashimoto, T. H. Hsieh, T. Kaneko, H. Matsufuru, J. Noaki, T. Onogi, E. Shintani and N. Yamada [JLQCD and TWQCD Collaborations], Phys. Rev. **D 80**, 034508 (2009).
[28] V. Gülpers, G. von Hippel and H. Wittig, Phys. Rev. **D 89**, 094503 (2014).
[29] B. Brandt, Int. J. Mod. Phys. **E 22**, 1330030 (2013).
[30] M. Engelhardt, B. Musch, P. Hägler, J. W. Negele and A. Schäfer, PoS **LATTICE2013**, 284 (2014).
[31] M. Engelhardt, B. Musch, P. Hägler, J. W. Negele and A. Schäfer, Int. J. Mod. Phys. Conf. Ser. **37**, 1560034 (2015).
[32] M. Engelhardt, B. Musch, P. Hägler, J. W. Negele and A. Schäfer, Few Body Syst. **56**, 447 (2015).
[33] F. Pijlman, Ph.D. thesis, Vrije Universiteit Amsterdam, 2006; arXiv:hep-ph/0604226.
[34] S. M. Aybat and T. C. Rogers, *Phys. Rev.* **D 83**, 114042 (2011).
[35] J. C. Collins, T. C. Rogers and A. M. Stasto, Phys. Rev. **D 77**, 085009 (2008).
[36] X. Ji, J.-P. Ma and F. Yuan, Phys. Rev. **D 71**, 034005 (2005).
[37] M. G. Echevarría, A. Idilbi and I. Scimemi, JHEP **07**, 002 (2012).
[38] J. Collins and T. Rogers, Phys. Rev. **D 87**, 034018 (2013).
[39] J. Collins and D. Soper, Nucl. Phys. **B193**, 381 (1981).
[40] S. M. Aybat, J. C. Collins, J.-W. Qiu and T. C. Rogers, Phys. Rev. **D 85**, 034043 (2012).
[41] J. P. Ralston and D. E. Soper, Nucl. Phys. **B152**, 109 (1979).
[42] R. D. Tangerman and P. J. Mulders, Phys. Rev. **D 51**, 3357 (1995).
[43] K. Goeke, A. Metz and M. Schlegel, Phys. Lett. **B618**, 90 (2005).
[44] D. Boer and P. J. Mulders, Phys. Rev. **D 57**, 5780 (1998).
[45] P. J. Mulders and R. D. Tangerman, Nucl. Phys. **B461**, 197 (1996).
[46] A. Bacchetta, D. Boer, M. Diehl and P. J. Mulders, JHEP **08**, 023 (2008).
[47] D. Boer, L. Gamberg, B. Musch and A. Prokudin, JHEP **1110**, 021 (2011).
[48] M. Aghasyan, H. Avakian, E. De Sanctis, L. Gamberg, M. Mirazita, B. Musch, A. Prokudin and P. Rossi, JHEP **1503**, 039 (2015).
[49] C. Aubin, C. Bernard, C. DeTar, J. Osborn, S. Gottlieb, E. Gregory, D. Toussaint, U. Heller, J. Hetrick and R. Sugar, Phys. Rev. **D 70**, 094505 (2004).
[50] P. Hägler *et al.* [LHP Collaboration], Phys. Rev. **D 77**, 094502 (2008).
[51] J. D. Bratt *et al.* [LHP Collaboration], Phys. Rev. **D 82**, 094502 (2010).
[52] M. Engelhardt, B. Musch, T. Bhattacharya, R. Gupta, P. Hägler, J. Negele, A. Pochinsky, A. Schäfer, S. Syritsyn and B. Yoon, PoS **LATTICE2014**, 167 (2015).
[53] J. Greensite, *An Introduction to the Confinement Problem* (Springer Lecture Notes in Physics, Vol. 821, 2011).
[54] M. Burkardt and B. Hannafious, Phys. Lett. **B658**, 130 (2008).
[55] R. G. Edwards and B. Joó [SciDAC Collaboration], Nucl. Phys. Proc. Suppl. **140**, 832 (2005).